Nanoscale Advances

Accepted Manuscript

This article can be cited before page numbers have been issued, to do this please use: M. Cercel, A. Nila, I. Smaranda, A. Androne, T. Burlanescu, A. Lorinczi, C. Negrila, E. Matei and M. Baibarac, *Nanoscale Adv.*, 2026, DOI: 10.1039/D5NA01164G.

ROYAL SOCIETY OF CHEMISTRY

rsc.li/nanoscale-advances

View Article Online
DOI: 10.1039/D5NA01164G

ARTICLE

Photochemical processes developed in the composites based on MoS_2, poly(ortho-toluidine), and reduced graphene oxide

Received 00th January 20xx,
Accepted 00th January 20xx

DOI: 10.1039/x0xx00000x

Madalina Cercel[1, 2], Andreea Nila[2], Ion Smaranda[2], Andreea Androne[2], Teodora Burlanescu[2], Adam Lörinczi[2], Catalin Negrila[2], Matei Elena[2] and Mihaela Baibarac[2*]

Using the solid-state interaction, the composites based on molybdenum disulfide (MoS_2), poly(ortho-toluidine) (POT), and reduced graphene oxide (RGO) were prepared. Raman scattering and FTIR spectroscopy studies have demonstrated that the interaction of the RGO and MoS_2 sheets with POT-emeraldine base state (EB) leads to composites of the type of RGO sheets non-covalently functionalized with POT pseudo-protonic doped with MoS_2 and RGO covalently functionalized with POT-leucoemeraldine salt (LS). An alternative way to prepare these composites is the solid-state interaction of the RGO and MoS_2 sheets with POT-emeraldine salt (ES), when composites of the type RGO non-covalently functionalized POT-salt having entities pseudo-protonic acidic doped in the presence of MoS_2, and RGO covalently functionalized with POT-leucoemeraldine base (LB) result. Using UV-VIS spectroscopy, we demonstrate that the exposure to UV light of these composites in protic polar solvents leads to the generation of POT-LB and POT-ES partially de-doped. The features of composites, after light exposure, as well as their transformation in the salt state, are highlighted by surface-enhanced Raman scattering. This study contributes to a better understanding of the properties of composites based on MoS_2, POT, and RGO, highlighting the need to avoid exposure to UV light of composites dissolved in polar protic solvents.

1. Introduction

In the last ten years, special attention has been paid to binary and ternary composites containing transition metal dichalcogenides such as MoS_2, WS_2, etc., reduced graphene oxide (RGO), and conducting polymers [e.g. 1, 2, 3]. The main targeted applications for these composites have been in the field of: i) supercapacitors [e.g. 4], ii) rechargeable lithium batteries [e.g. 5], iii) rechargeable sodium batteries [e.g. 6], iv) aptasensors for the detection of aflatoxin B1 [7], v) electrochemical sensors for simultaneous detection of ascorbic acid, dopamine, and uric acid [8], vi) layers in OLEDs [9], vii) Li-S batteries [10], ix) immunosensors [11]; and last but not least x) in photocatalysis as an antipollution and antimicrobial agent [12]. The most commonly used polymers for the preparation of these composites were polypyrrole [5] and polyaniline [e.g. 4]. A first work on composites based on poly(o-toluidine) (POT) and MoS_2 and WS_2-type TMDs was reported in 2025 [3]. Considering that POT is a polyaniline that has benzene and quinoid rings substituted with a methyl group, in the following, we will review the main methods used for the synthesis of MoS_2/PANI/RGO composites. Four methods were used to obtain ternary composites of the type MoS_2/PANI/RGO as follows: i) hydrothermal synthesis of MoS_2 in the presence of graphene oxide (GO), resulting in the MoS_2/RGO composite, a reaction followed by the in situ polymerization reaction of aniline in the presence of HCl and ammonium persulfate (APS) [4]; ii) polymerization of aniline in the presence of APS and exfoliated graphene and MoS_2 leading to the obtaining of PANI/graphene/MoS_2 composites, having intercalated structures of graphene and MoS_2 layers that are encapsulated in PANI [13]; iii) hydrothermal synthesis of the MoS_2/RGO binary composite, followed by chemical polymerization of aniline in the presence of the MoS_2/RGO binary composite, using APS as an oxidizing agent, resulting in a ternary MoS_2/RGO/PANI composite, in which the PANI concentration can vary between 50-80 wt.%; PANI adsorption on the surface of the MoS_2/RGO binary composite occurs through electrostatic interactions established between the structure of the MoS_2/RGO composite and PANI [14]; and iv) 3D MoS_x-PANI@RGO composites were prepared by the hydrothermal method. To achieve these, GO was used as a precursor for RGO, acting as a catalyst for the synthesis of MoS_x nanoparticles as well as an acidic dopant for the PANI–emeraldine base [15]. In comparison with this progress, in this work for the preparation of the MoS_2/POT/RGO composites, interaction in the solid state will be used, POT being both as emeraldine base (EB) and emeraldine salt (ES). In this context, it should be mentioned that similar to PANI, POT in the semiconducting state can exist in three forms known as leucoemeraldine base (LB), emeraldine base (EB) and pernigranilane base (PB), the difference between them consists in the structural units that contain in the case of: a) LB four benzene rings and four amine groups; b) EB three

[1.] University of Bucharest, Faculty of Physics, Atomistilor Street 405A, Magurele, Romania.
[2.] National Institute of Materials Physics, Laboratory of Optical Processes in Nanostructured Materials, Atomistilor street 405A, Magurele, Romania. E-mail: barac@infim.ro
Supplementary Information available: [details of any supplementary information available should be included here]. See DOI: 10.1039/x0xx00000x

benzene rings, a quinoid ring, two amine groups and two imine groups and c) PB two benzene rings, two quinoid rings and four imine groups. The conductive forms of POT are known as leucoemeraldine salt (LS), emeraldine salt (ES), and pernigranilane salt (PS) [16, 17]. They are characterized by the presence of the protonated or pseudo-protonic structures. The transition from the semiconducting to the conducting state of POT can be performed similarly to PANI by: i) acidic protonic doping, which involves the use of an acid such as H_2SO_4, HCl, etc., with the generation of the protonated structure on the macromolecular chain, b) redox doping, which involves reactions in which the dopant moves or brings electrons from or to the conductive polymer, leading to a p- or n-type doping and c) pseudo-acidic protonic doping which takes place in the presence of organic or inorganic salts such as tetrabutylammonium tetrafluoroborate, heavy metal sulfides, etc. [16, 17]. Although important progress is reported in the case of MoS_2/PANI/RGO composites, little information exists about the chemical interactions that take place at the interface of the three constituents, which may have important consequences on the physicochemical properties and, implicitly, on the applications envisaged to be developed using such materials. In this work, a detailed understanding of the interactions that take place during the preparation of composites starting from MoS_2, RGO, and POT will be presented through correlated studies of X-ray diffraction (XRD), Raman scattering, FTIR spectroscopy, and, finally, UV-VIS spectroscopy. The behavior of these composites in the presence of polar and non-polar solvents, as well as of light emitted by a halogen source, will also be reported. To highlight the photochemical reaction products of binary and ternary composites, SERS studies will be presented.

To the best of our knowledge, no studies have reported MoS_2/RGO/POT ternary composites prepared via solid-state interaction, nor a detailed spectroscopic investigation of the interfacial interactions and photochemical behavior of such systems. A comparative analysis of the progress reported in the case of MoS_2/RGO/conducting polymer composites is shown in Table 1. Considering this progress, the novelty of the present study can be outlined more clearly: i) although a significant number of studies have been devoted to MoS_2/RGO composites incorporating conducting polymers such as polyaniline (PANI) and polypyrrole (PPY), the use of poly(o-toluidine) (POT) remains largely unexplored in ternary systems. Given that POT is a methyl-substituted derivative of PANI, its structural particularities are expected to influence both the electronic properties and the interfacial interactions within the composite;

ii) in contrast to the commonly reported hydrothermal synthesis followed by in situ oxidative polymerization, the composites in this work are prepared via solid-state interaction. This approach avoids the use of oxidizing agents and may lead to distinct interfacial organization and interaction mechanisms.

iii) while most previous reports primarily focus on electrochemical applications (e.g., supercapacitors, batteries, sensors), the present study is centered on a detailed investigation of the physicochemical interactions between MoS_2, RGO, and POT. This is achieved through a correlated analysis using XRD, Raman, FTIR, and UV–Vis spectroscopy, iv) additional insight is provided through the study of the behavior of these composites in polar and non-polar solvents, as well as under halogen light irradiation. The use of SERS to identify photochemical reaction products further distinguishes this work from previously reported studies.

Table 1. Comparative analysis of MoS_2/RGO/conducting polymer composites

Composite Ref.	Polymer	Synthesis way	Main topic	Key limitation
MoS_2/RGO/PANI [4]	PANI	Hydrothermal and in situ polymerization	Supercapacitor performance	Limited interfacial analysis
Graphene/MoS_2/PANI [13]	PANI	Chemical polymerization using exfoliated phases	Electrode materials	Morphology/Performance
MoS_2/RGO/PANI [14]	PANI	Hydrothermal and oxidative polymerization	Electrochemical behavior	Weak insight into interactions
MoSx/PANI@RGO [15]	PANI	Hydrothermal (3D aerogel)	Energy storage	No detailed spectroscopic correlation
MoS_2/GNP/PANI [18]	PANI/PPY	Melt + exfoliation	Supercapacitors	Application-driven
MoS_2/GNP/PANI [5]	PANI/PPY	Melt + exfoliation	Supercapacitors	Application-driven
CNT/PANI@MoS_2[19]	PANI	Hydrothermal	Structure–property	No RGO
PANI/MoS_2 [20]	PANI	Hydrothermal	Adsorption	Binary system
PANI/MoS_2 [21]	PANI	Mixture	Supercapacitors	No RGO
PANI/RGO [22]	PANI	Chemical/Electrochemical polymerization	Supercapacitors	No MoS_2
POT/MoS_2:WS_2 [3]	POT	Mixture	Electrical properties	No RGO
POT/RGO [23]	POT	Solid-state reaction	Supercapacitors	No MoS_2
MoS_2/RGO/POT [This work]	POT	Solid-state reaction	Interfacial interactions and photochemical behavior	MoS_2/RGO/POT

View Article Online
DOI: 10.1039/D5NA01164G

2. Experimental

The following compounds: molybdenum disulfide (MoS_2), reduced graphene oxide (RGO), o-toluidine (≥99%, OT), N-methyl-2- pyrrolidone (NMP), N, N'-dimethylformamide (DMF), acetone, toluene, potassium dichromate ($K_2Cr_2O_7$), sulfuric acid (H_2SO_4 95.0-98.0%%), acetonitrile (CH_3CN, ≥99.5%,), Au nanoparticles with an average size of 10 nm and ammonia solution (NH_4OH 28-30%) were purchased from Merck company.

To prepare the composites, MoS_2 layers were prepared by mechanical exfoliation using the ball milling method, with 1 g of MoS_2 particles being placed in a PM 100 – RETSCH ball mill and ground at 600 rpm for one hour. This exfoliation technique provides a high yield and has economic sustainability, while the structural defects produced on the layer surfaces/edges are beneficial in various applications such as energy storage [24].

POT-ES was prepared by in-situ chemical polymerization of OT, according to Ref. [3]. According to our previous study, the interaction of POT-ES with NH_4OH allowed us to obtain POT-EB [3]. Four other samples were prepared, starting from a mixture of the three constituents, i.e., MoS_2, POT-EB/POT-ES, and RGO, having the concentration of the three compounds equal to: i) 50 wt.%, 25 wt.%, and 25 wt.%, labelled as MoS_2/POT-EB/RGO 50: 25: 25, ii) 50 wt.%, 40 wt.%, and 10 wt.%, labelled as MoS_2/POT-EB/RGO 50: 40: 10, iii) 50 wt.%, 25 wt.%, and 25 wt.%, labelled as MoS_2/POT-ES/RGO 50: 25: 25, ii) 50 wt.%, 40 wt.%, and 10 wt.%, labelled as MoS_2/POT-ES/RGO 50: 40: 10. The solid-state interaction of each reaction mixture took place by grinding for 30 min. Using the same protocol, the following binary composites RGO/MoS_2, POT-EB/MoS_2, and POT-ES/MoS_2, with a MoS_2 concentration of 25 wt.%, were prepared.

The characterization of the MoS_2/POT-EB/RGO and MoS_2/POT-ES/RGO composites was performed by X-ray diffraction (XRD), Raman scattering, FTIR spectroscopy, and UV-VIS spectroscopy. XRD diagrams of MoS_2/POT-ES/RGO composites were recorded with Bruker's D8 Advance X-ray diffractometer.

Raman spectra of the MoS_2/POT-EB/RGO and MoS_2/POT-ES/RGO composites were recorded at an excitation wavelength of 1064 nm, using a Bruker FTRaman spectrophotometer, model MultiRam.

FTIR spectra of the MoS_2/POT-EB/RGO and MoS_2/POT-ES/RGO composites were recorded using a Bruker Vertex 80 FTIR spectrophotometer.

UV-VIS spectra of MoS_2/POT-EB/RGO and MoS_2/POT-ES/RGO composites were recorded with the UV-VIS-NIR spectrophotometer, Lambda 950, from Perkin Elmer.

For the photochemical processes of the MoS_2/POT-EB/RGO and MoS_2/POT-ES/RGO composites, a halogen lamp with a power of 100 W was used. The distance between the halogen lamp and the quartz cuves containing the solutions of the MoS_2/POT-EB/RGO and MoS_2/POT-ES/RGO composites in NMP, with the concentration of 0.2 mg/ml, was 10 cm. The products of photochemical reactions were highlighted by surface-enhanced Raman scattering (SERS), using as Au nanoparticles as plasmonic substrates.

X-ray photoelectron spectroscopy (XPS) spectra of the polymers POT-EB and POT-ES, as well as the MoS_2/POT-EB/RGO and MoS_2/POT-ES/RGO composites, a SPECS spectrometer endowed with a Phoibos 150 electron energy analyzer and a monochromatic X-ray source consisting of an aluminum anode (Al Kα 1486.74 eV).

Scanning electron microscopy (SEM) images of the MoS_2/POT-EB/RGO and MoS_2/POT-ES/RGO composites were recorded with a Zeiss Gemini 500 field-emission scanning electron microscope.

3. Results and Discussion

3.1 Structural and vibrational properties of the composites based on MoS_2, POT, and RGO

Figure 1 shows the XRD diagrams in the case of MoS_2 and the MoS_2/POT-ES/RGO 50:40:10 and MoS_2/POT-ES/RGO 50:25:25 composites.

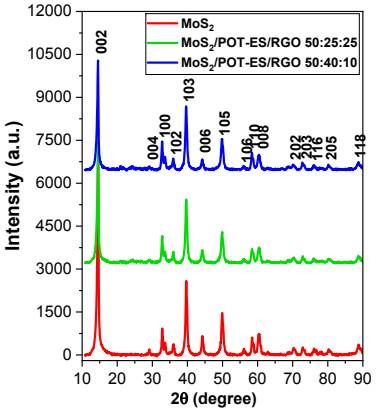

Figure 1. XRD diagrams of MoS_2 (red curve) and the MoS_2/POT-ES/RGO 50:25:25 (green curve) and MoS_2/POT-ES/RGO 50:40:10 (blue curve) composites.

According to Figure 1, it can be observed that all XRD diagrams are characterized by an intense maximum located at 2θ =14.6°, which is assigned to the (002) crystal plane, this maximum being accompanied by other lower intensity maxima which are located at 2θ = 29.1°, 32.8°, 33.6°, 35.9°, 39.7°, 44.3°, 49.9°, 56°, 58.4°, 60.5°, 70.3°, 72.8°, 76°, 78.2°, 80.3°, and 88.7°, they being assigned to the crystalline planes (004), (100), (101), (102), (103), (006), (105), (106), (110), (008), (202), (2030, (116), (204), (205) and (118) of the 2H phase of MoS_2 [PDF-04-003-3080]. Knowing that the (002) crystal plane corresponds to the basal planes, i.e. the superimposed S-Mo-S layers and the (103) crystal plane corresponds to the non-basal planes, which reflect the crystalline order in a different direction than that of the two-dimensional layer structure, we note that a change in the ratios of the intensities of the peaks assigned to the crystalline planes (002) and (103) occurs from 2.84 to 1.93 and 1.74 in the

View Article Online DOI: 10.1039/D5NA01164E

case of MoS_2 and composites MoS_2/POT-ES/RGO 50:25:25 and MoS2/POT-ES/RGO 50:40:10, respectively. This experimental result can be interpreted as a consequence of the fact that: a) the mass ratio of MoS_2 is diluted 50% in the POT-ES and RGO-containing compositions according to the compositional ratios. As such, the drop of the intensities corresponding to the (002) planes to about 50% in the latter two compositions compared to the pure MoS_2 is understandable considering the large difference in electron density (Z number) of the compared compositions; b) the change of the intensity ratios of the (002) and (103) planes mentioned above suggests that the shape - or the aspect ratio - of the nanocomposite's crystallites changes as well during this compositional dilution, most probably due to the presence of more-and-more POT-ES. The contribution of the RGO in this sense appears not to be detectable. Similar relative intensity changes one may notice for peaks of other planes as well, sustaining the shape change of the crystallites in the composites, and c) possible defects appeared during the preparation.

Figure 2 shows the SEM images of the MoS_2/POT-EB/RGO and MoS_2/POT-ES/RGO composites. Figure 2a highlights the crumpled RGO large sheets, MoS_2 platelets with diameters ranging between 134-687 nm, as well as POT-EB particles with diameters between 24-39 nm, which mostly appear in agglomerated form. Figure 2b highlights crumpled RGO large sheets, MoS_2 platelets with diameters ranging between 121-377 nm, and isolated POT-ES particles with diameters between 21.2 – 38.2 nm. The MoS_2 platelets show a diameter between 115 nm and 1.088 µm (Figure 2c).

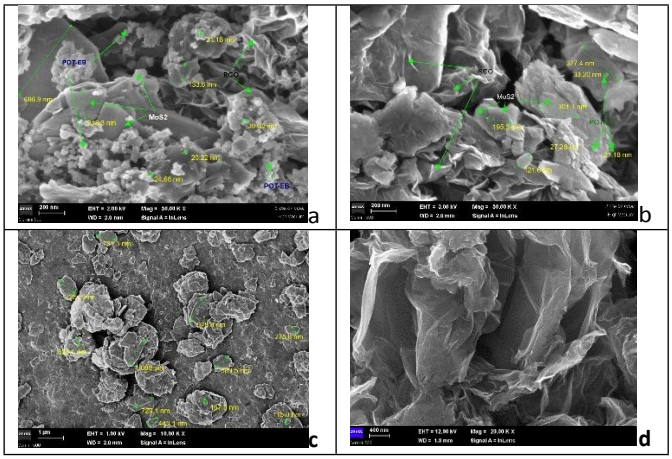

Figure 2. SEM images of the MoS_2/POT-EB/RGO (a) and MoS_2/POT-ES/RGO (b) composites, as well as MoS_2 (c) and RGO sheets (d)

An explanation for the small size of MoS_2 sheets in the composites with POT-EB/POT-ES and RGO must consider the synergy between the mechanical fragmentation induced by the grinding process and the exfoliation assisted by solid-solid interactions with the macromolecular compounds and RGO. The macromolecular chains of POT-EB/POT-ES reduce the cohesion of the MoS_2 interlayers, while the RGO layers stabilize the exfoliated fragments, preventing their re-agglomeration. A consequence of these two effects is that, in the composites, MoS_2 flakes are significantly smaller than the starting material. As observed in Figure 2d, the RGO layers are crumpled.

To understand the potential interactions between the three constituents, Figures 3 and 4 show the Raman and FTIR spectra of the MoS_2: POT-ES: RGO and MoS_2: POT-EB: RGO composites.

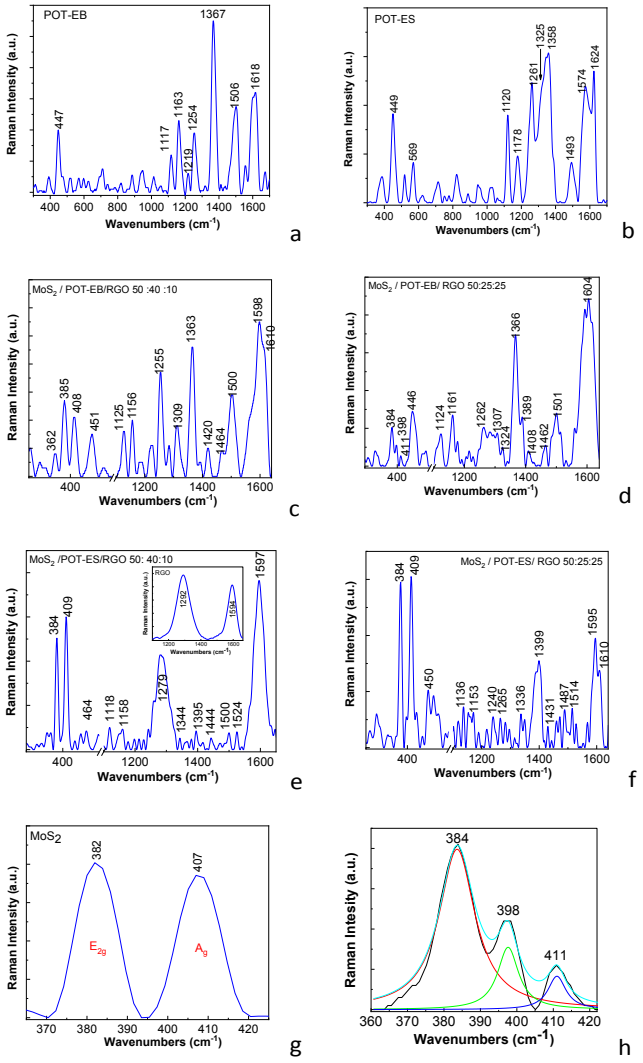

Figure 3. Raman spectra of the composites POT-EB (a), POT-ES (b), MoS_2/POT-EB/RGO 50:40:10 (c), MoS_2/POT-EB/RGO 50:25:25 (d), MoS_2/POT-ES/RGO 50:40:10 (e), MoS_2/POT-ES/RGO 50:25:25 (f), MoS_2 (g), and deconvolution of the Raman spectrum of MoS_2/POT-EB/RGO 50:25:25 (h). The insert of Fig. (e) corresponds to the Raman spectrum of RGO.

Figure 3a highlights the following Raman lines of POT-EB which are peaked at 447, 1117, 1163, 1219, 1254, 1367, 1506 and 1618 cm^{-1}, they being assigned to the vibrational modes of deformation of aromatic ring, deformation of benzene ring (B) + bending C-H in CH_3 group, bending C-H in B ring, stretching C-N + stretching C-C + bending C-H in Bring, stretching C-C in B ring, stretching C-C in quinoid (Q) ring + bending C-H in B ring, stretching C=N and stretching C+C + bending C-H in B ring [1, 25]. Figure 3b highlights the Raman lines of POT-ES located at

1178, 1261, 1325-1358, 1493, 1574, and 1624 cm^{-1}, which were assigned to the vibrational modes of C-H in-plane deformation, C-N bond stretching in the Q ring, C-N bond stretching in B-NH^{+}=Q, C-C + C-H + N-H bond stretching, N=Q=N structure, and C-C + C-H bond stretching [26]. In the case of the Raman spectra of the composites MoS_2/ POT-EB/ RGO 50:40:10 and MoS_2/ POT-EB/ RGO 50:25:25 one observes: a) the Raman lines situated at 1363-1366, 1500-1501, and 1598-1604 $cm^{-1,}$ which belong to POT-EB; and b) the Raman lines peaked at 384-385 and 408-411 cm^{-1}, assigned to the vibrational mode E_{2g} and A_g of MoS_2 which belong to the in-plane vibrations of the two sulfur atoms and respectively to the out-of-plane vibrations of the S atoms in opposite directions [27]. The ratio between the intensities of the two Raman lines at 384-385 and 408-411 cm^{-1} ($I_{384-385}/I_{408-411}$), in the case of the MoS_2/POT-EB/RGO 50:40:10 and MoS_2/POT-EB/RGO 50:25:25 composites, is equal to 3.73 (Figure 3c) and 1.28 (Figure 3d), indicating an exfoliation process, which weakens the interlayer interactions of MoS2. An important role in the exfoliation process of MoS_2 is played by POT-EB, an assertion supported by the value of the $I_{383-385}/I_{408-410}$ ratio, which in the case of the POT-EB/MoS_2 composite is equal to 1.125 (Figure S1b). For POT-EB-based composites, the I_{E2g}/I_{Ag} ratio increases compared to that of MoS_2, being equal to 0.97 (Figure 3e). This behavior may suggest a change in interlayer interactions. However, this change cannot be attributed exclusively to exfoliation. It may also reflect differences in dispersion, local structure, or interaction with POT-EB and RGO. In the case of the Raman spectra of the MoS_2/POT-ES/RGO 50:40:10 and MoS_2/POT-ES/RGO 50:25:25 composites, the presence of POT-ES Raman lines located at 1279-1265, 1343/1336-1395/1399, 1500-1493, 1597-1595 and 1624 cm^{-1} [26], as well as the MoS2 Raman line located at 384 and 409 cm^{-1} [3]. The ratio between the intensities of the Raman lines peaking at 384 and 409 cm^{-1} in the case of MoS_2/POT-ES/RGO composites is equal to 0.97 (Figure 3e) and 0.84 (Figure 3f), lower than that reported for MoS_2 particles (Figure 3g) or than in the case of POT-ES/MoS_2 and RGO/MoS_2 composites, which have the ratio value equal to 1.64 (Figure S1c) and 1.71 (Figure S1a), respectively. This decrease could be associated with a weakening of the interlayer coupling. Such an effect is often correlated with exfoliation or increased disorder in the MoS_2 layers. However, the opposite trends observed for the POT-EB and POT-ES systems indicate that the intensity ratio alone cannot be used as a direct or universal measure of the degree of exfoliation in these composites. The Raman response is likely influenced by several factors, including charge transfer, defect density, and polymer-MoS_2 interactions. In addition, since the composites were prepared by solid-state milling, the extent of exfoliation is expected to be limited. Therefore, the observed spectral changes are more reasonably attributed to structural disorder and interfacial interactions than to a well-defined exfoliation process. However, this change cannot be attributed solely to exfoliation. It may also reflect differences in dispersion, local structure, or interaction with POT-EB and RGO.

Unlike the Raman spectrum of graphene recorded at an excitation wavelength of 532 nm (2.33 eV), when the D band maximum is located at 1350 cm^{-1} [28], the Raman spectrum of RGO recorded at an excitation wavelength of 1064 nm (1.16 eV) has the D band maximum located at 1290 cm^{-1}. This result is in good agreement with the previous study on the dependence of the D band on the excitation wavelength [29] and with the Raman studies reported at an excitation wavelength of 1064 nm [30]. Knowing that the D and G bands of RGO are located at 1290 and 1598 cm^{-1}, associated with the defects visualized by the presence of carbon atoms with sp^3 hybridization and carbon atoms with sp^2 hybridization, respectively [31], and that POT-ES presents a Raman line at 1261 cm^{-1}, in the case of the two MoS_2 /POT-ES/RGO composites it is observed that the D band of RGO is positioned at 1265 cm^{-1} (Figure 3f) and 1279 cm^{-1} (Figure 3e), which indicates a tension in the basal plane of RGO as a consequence of an adsorption on a more rigid structure of the polymer generated by its interaction with MoS_2. Other changes observed in Figure 3 concern the shift of the Raman line from 1178 cm^{-1} of PANI-ES (Figure 3f) to 1158 cm^{-1} (Figure 3d) and 1153 cm^{-1} (Figure 3b). This result indicates a change in the component of the structural units of the type emeraldine in leucoemeraldine, the latter presenting in the Raman spectrum a line at 1157 cm^{-1} associated with the C-H vibrational mode [32].

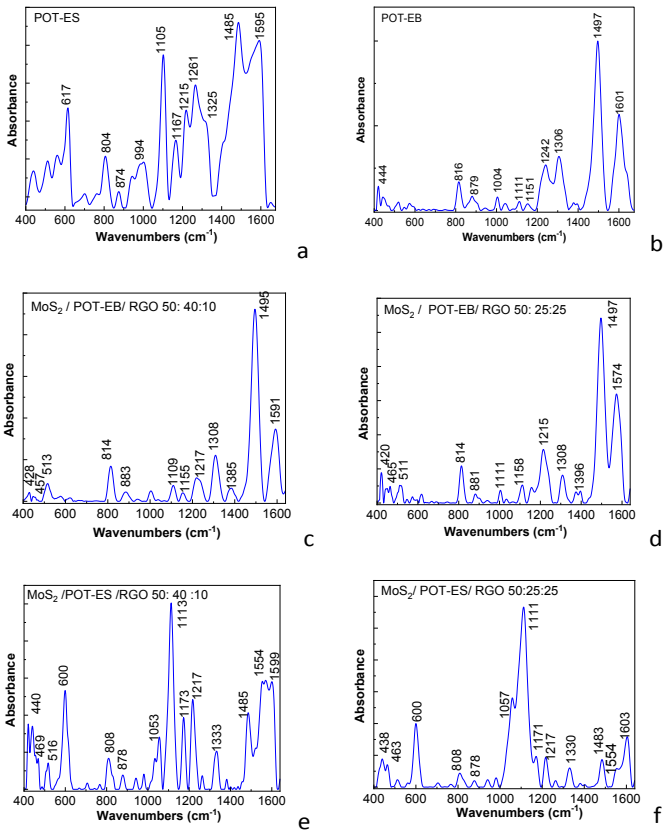

Figure 4. FTIR spectra of POT-ES (a), POT-EB (b), MoS_2/POT-EB/ RGO 50:40:10 (c), MoS_2/POT-EB/ RGO 50:25:25 (d), MoS_2/POT-ES/ RGO 50:40:10 (e), and MoS_2/POT-ES/ RGO 50:40:10 (f).

In order to explain these variations, Figure 4 highlights the FTIR spectra of MoS_2/POT-EB/RGO and MoS_2/POT-ES/RGO. According to Figure 4, the FTIR spectra of: a) POT-ES shows IR bands located at 994, 1105, 1167, 1261, 1325, 1485 and 1595 cm^{-1} (Figure 4a), assigned to vibrational modes of deformation of the benzene ring, deformation of the benzene ring + C-H, the C-H bond in the quinoid ring, stretching of the C-N bond in the B-NH^+=Q entity, stretching of the C-N bond in the vicinity of the quinoid ring, stretching of the C-C + C-H + N-H bonds and the N-H bond in the N=Q=N structure [25, 33, 34]; b) POT-EB shows IR bands located at 1004, 1111, 1151, 1242, 1306, 1497 and 1601 cm^{-1} (Figure 4b) assigned to the vibrational modes of deformation of the benzene ring (B), of deformation of B + C-H, of the C-H bond in the quinoid ring (Q), of stretching of the C-N bond in the B-N=Q entity, of stretching of the C-N bond in the vicinity of Q, of stretching of the C-C + C-H + N-H bonds and of the N-H bond in the N=Q=N structure, respectively [25, 33]; c) the MoS_2/POT-ES/RGO 50:40:10 and MoS_2/POT-ES/RGO 50:25:25 composites, the IR bands of POT are shifted from 617, 1105, 1325 and 1595 cm^{-1} (Figure 4a) to 600, 1113–1111, 1333–1330 and 1599-1603 cm^{-1} (Figures 4e and 4f), simultaneously with changes in their absorbance and the presence of a new IR band at ca. 1053-1057 cm^{-1} which belongs to the symmetric vibrational mode of the S-O bond in HSO_4^- ions [35]. According to vibrational studies reported by S. Quillard et al. [25], the polyaniline class compounds to which POT is related in the form of LB exhibit IR bands at ca. 1118, and 1603 cm^{-1}, which were assigned to the B_{2u} and B_{3g} vibrational modes, while the N-N'-diphenyl-1, 4-phenylene diamine structural units in LB exhibit IR bands at 600 and 1331 cm^{-1}, these bands being close to those present in the FTIR spectra of the MoS_2/POT-ES/RGO composites at 600, 1111–1113, 1330–1333 and 1603–1599 cm^{-1}. An interesting fact noted in Figure S2b is that the IR bands assigned to the B_{2u} and B_{3g} vibrational modes are also observed in the IR spectrum of the composite resulting from the interaction of POT-EB with MoS_2, these being located at 1115 and 1601 cm^{-1}. Early studies reported by Z. Ping et al. [36], demonstrated that PANI in the form of LS exhibits IR bands at 1336 and 1606 cm^{-1} which are also close to those reported for MoS_2/POT-ES/RGO composites mentioned to be located at 1330–1333 and 1603–1599 cm^{-1}; in the case of the FTIR spectrum of the composite resulting from the interaction of POT-ES with MoS_2, it is observed that the two IR bands are located at 1338 and 1610 cm^{-1} (Figure S2c). and d) the MoS_2/POT-EB/RGO 50:40:10 and MoS_2/POT-EB/RGO 50:25:25 composites, IR bands belonging to POT are shown, which have IR bands at 1242 and 1601 cm^{-1} (Figure 4b) shifted to 1217–1215 and 1591–1574 cm^{-1}, respectively (Figures 4c and 4d). The presence of IR bands at 1591 and 1215 cm^{-1} indicates an interaction at the POT-EB interface with MoS_2 and RGO, leading to a partial transformation of POT-EB into POT-ES. Considering these changes illustrated by IR spectroscopy and Raman scattering, the solid-state reaction of POT-EB and POT-ES, respectively, with MoS_2 and RGO can take place according to Figure 5.

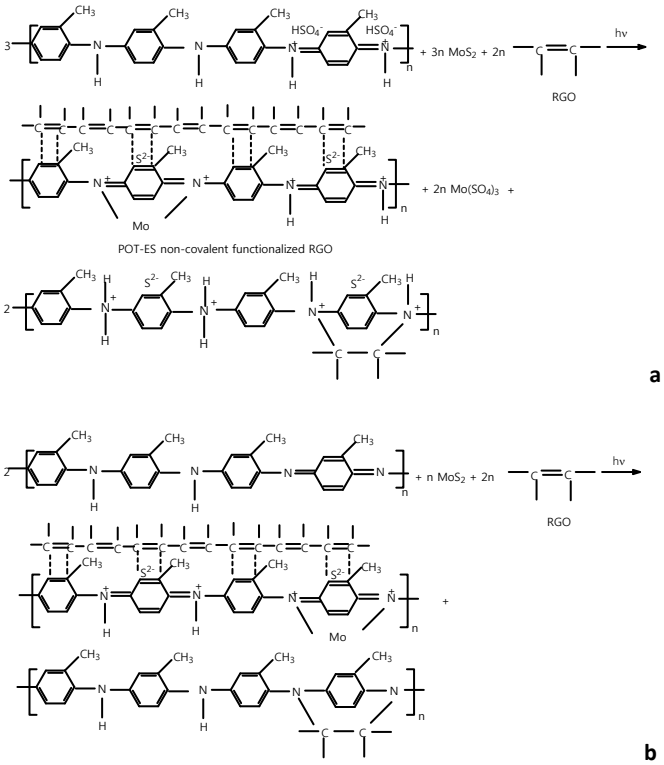

Figure 5. The interaction of: a) POT-ES with MoS_2 and RGO; and b) POT-EB with MoS_2 and RGO.

In our opinion, Figure 5 highlights that the reaction products of a) POT-ES with MoS_2 and RGO correspond to a ternary composite (TC) of the type RGO non-covalent functionalized with POT pseudo-protonic doped in the presence of MoS_2, and a binary composite (BC) of the type RGO covalently functionalized with POT-LS; and b) POT-EB with MoS_2 and RGO correspond to TC of the type RGO non-covalent functionalized with POT pseudo-protonic doped in the presence of MoS_2, and BC of the type RGO covalently functionalized with POT-LB.
A schematic representation of the reaction products presented above is illustrated in Figure 6.

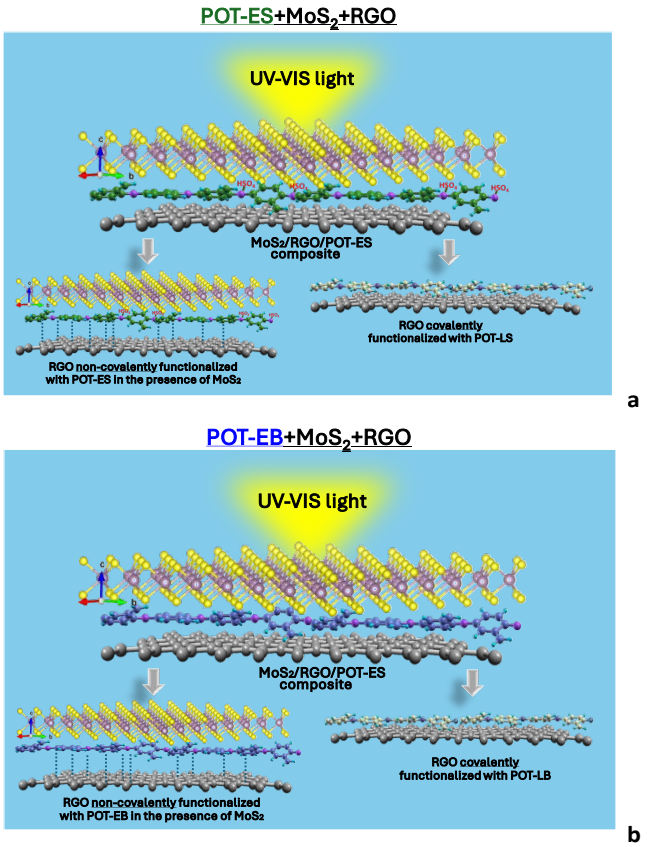

Figure 6. Schematic representation of the reaction products resulting from the interaction of a) POT-ES with MoS_2 and RGO; and b) POT-EB with MoS_2 and RGO.

Figure S2a shows the FTIR spectrum of MoS_2, which is characterized by an intense IR band at 469 cm^{-1}, assigned to the in-plane asymmetrical vibration of Mo and S atoms, with A_{2u} symmetry [37]. This IR band in the case of the composites MoS_2/POT-EB/RGO 50:40:10 (Figure 4c), MoS_2/POT-ES/RGO 50:40:10 (Figure 4d), MoS_2/POT-EB/RGO 50:25:25 (Figure 4e), MoS_2/POT-ES/RGO 50:25:25 (Figure 4f), POT-EB/MoS_2 (Figure S2b), and POT-ES/MoS_2 (Figure S2c) is peaked at 469, 457, 463, 465, 469, and 469 cm^{-1}. The shift of the IR band maximum attributed to the vibrational modes of MoS_2, observed only in the ternary composites MoS_2/POT-EB/RGO and MoS_2/POT-ES/RGO, indicates a significant modification of the electronic and structural environment of MoS_2. The presence of RGO favors the formation of an electronic coupling network between MoS_2 and the POT chains (especially in the salt form), which leads to charge transfer and/or local strains on the Mo–S network. Other proofs that support Figure 5 are shown in the following by XPS studies. Figure 7 presents the XPS spectra of the macromolecular compounds POT-EB and POT-ES, as well as the composites MoS_2/POT-EB/RGO 50:25:25, and MoS_2/POT-ES/RGO 50:25:25

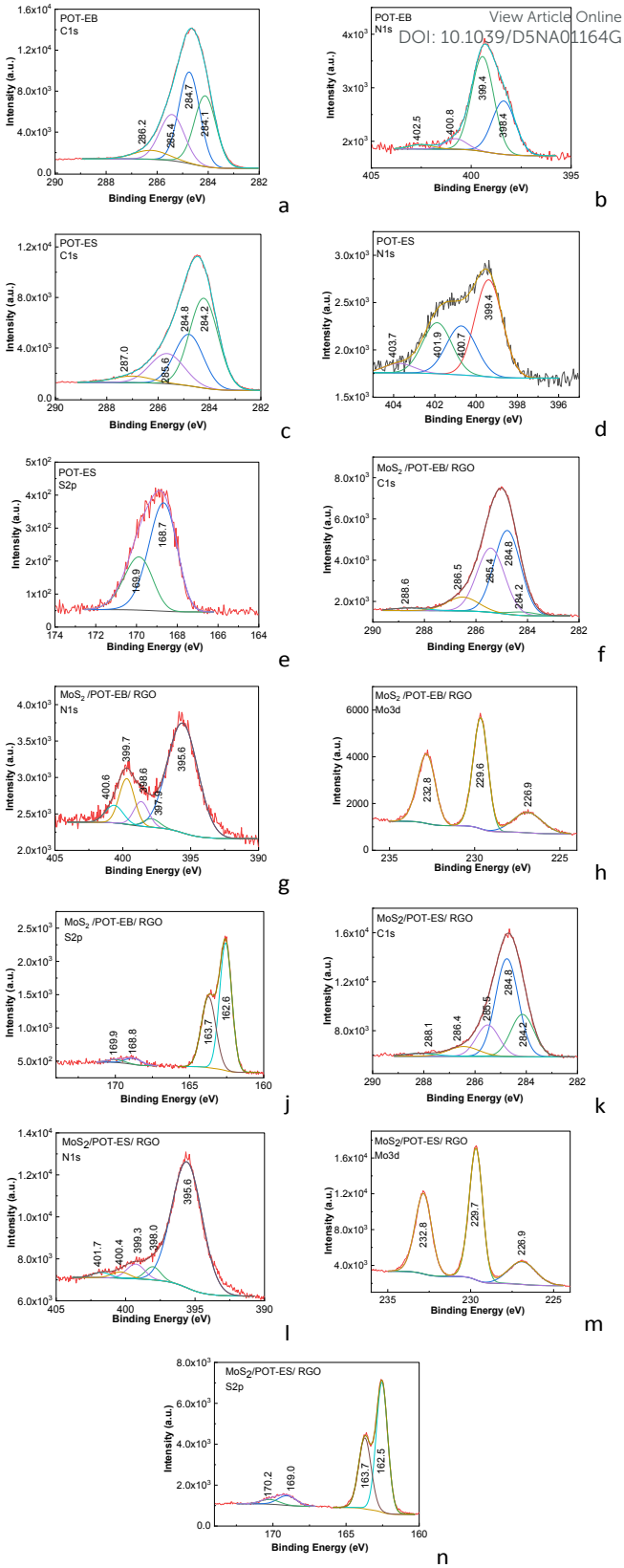

Figure 7. XPS C1s, N1s, Mo3d, and S2p spectra of POT-EB (a, b), POT-ES (c, d, e), MoS_2/POT-EB/ RGO 50:25:25 (f, g, h, j), and MoS_2/POT-ES/ RGO 50:25:25 (k, l, m, n).

Figures 7a-7d highlights in the case of the deconvolution of: i) the XPS C1s spectrum of POT-EB, four bands peaked at 284.1, 284.7, 285.4, and 286.2 eV, assigned to the bonds C=C, C-C/C-H, C-N/C=N, and C-O-H [38], while the bands of the deconvoluted XPS C1s spectrum of POT-ES are situated at 284.2, 284.8, 285.6, and 287 eV; the change of the ratio between the area of the peaks assigned to the C=C and C-C/C-H bonds from 0.82 to 1.73 is a consequence of the protonated structure of POT-ES; and ii) the XPS N1s spectrum of POT-EB, two bands of high intensity peaked at 398.4, and 399.4, eV, attributed to the bonds of the type imine (C=N-C) and amine (C-NH-C), accompanied of two bands of low intensity at 400.8 and 402.5 eV assigned to protonated amine ($-NH_2^+$) and protonated imine C-NH^+=C, respectively [39]. The deconvolution of the XPS N1s spectrum of POT-ES highlights three bands of high intensity, peaked at 399.4, 400.7, 401.9 eV, accompanied by a band of low intensity at 403.7 eV.

Figures 7e-7n highlight, in the case of the deconvolution of: i) the XPS C1s spectra of the MoS_2/POT-EB/ RGO 50:25:25 and MoS_2/POT-ES/ RGO 50:25:25 composites, five bands at 284.8, 284.2, 285.4-285.5, 286.5, and 288.6-288.1 eV, having the ratio between the area of the peaks assigned to the C=C and C-C/C-H bonds equal to 0.04 and 0.44, respectively. This decrease is a consequence of the covalent functionalization of RGO with POT-LB (Figure 5b) and POT-LS (Figure 5a), respectively. ii) the XPS N1s spectra of the MoS_2/POT-EB/ RGO 50:25:25 and MoS_2/POT-ES/ RGO 50:25:25 composites, five bands at 395.6, 397.9-398.0, 398.6-399.3, 399.7-400.4, and 400.6-401.7 eV, assigned to the bonds C-N^+(R)=C (R = Mo, as $Mo3p_{3/2}$), C=N-C, C-NH-C, -NH_2^+- and C-NH^+=C, respectively [39]; the presence of the band at 395.6 eV must to correlated to the reaction product of the type RGO non-covalent functionalized with POT pseudo-protonic doped in the presence of MoS_2 show in Figures 5a and 5b; iii) the XPS Mo3d spectra of the MoS_2/POT-EB/ RGO 50:25:25 and MoS_2/POT-ES/ RGO 50:25:25 composites, three bands at 226.9, 229.7 and 232.8 eV are remarked, they being assigned to S2s in sulfide, $Mo3d_{5/2}$ in sulphide (Mo^{4+}) and $Mo3d_{5/2}$ in sulphate or Mo^{6+} $3d_{5/2}$ [40,41]; and iv) the XPS S2p spectra of the MoS_2/POT-EB/ RGO 50:25:25 and MoS_2/POT-ES/ RGO 50:25:25 composites, four bands peaked at 168.8-169, 169.9-170.2, 162.6-162.5 and 163.7 eV, assigned to $S2p_{3/2}$ and $S2p_{1/2}$ of S-O bond of molybdenum sulfate, $S2p_{3/2}$ of Mo-S bond and $S2p_{3/2}$ of S-C bond [29, 41].

3.2 Photochemical processes of the composites based on MoS_2, POT, and RGO

Figure 8 shows the UV-VIS spectra of the solutions of MoS_2/POT-EB/RGO and MoS_2/POT-ES/RGO, both in NMP, having a concentration of 0.2 mg/ml, and their evolution by exposure to a light emitted by a halogen lamp.

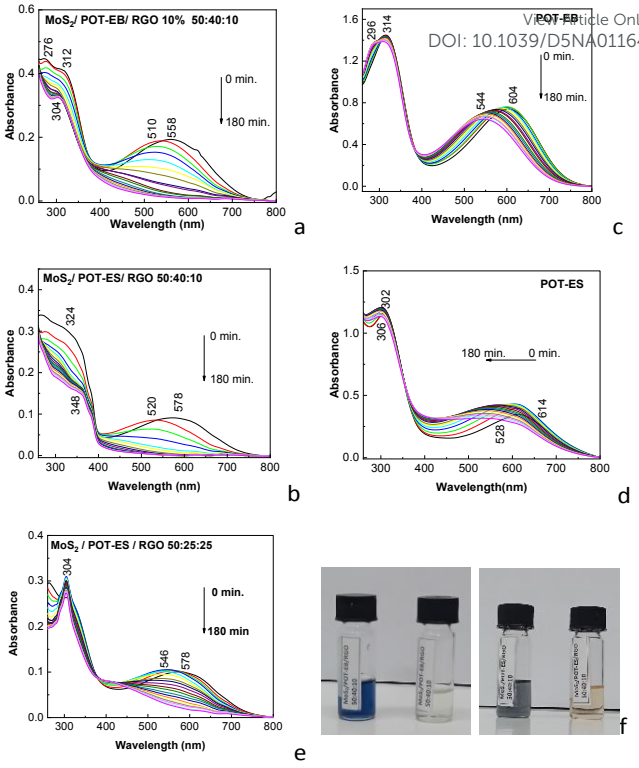

Figure 8. UV-VIS spectra of the composites MoS_2/POT-EB/RGO 50:40:10 (a) and MoS_2/POT-ES/RGO 50:40:10 (b), and conjugated polymers POT-EB (c) and POT-ES (d), as well as MoS_2/ POT-ES/ RGO 50:25:25 (e) in NMP and their evolution by exposure to a light emitted by a halogen lamp, for 180 min. Figure f shows the color changes of the composites MoS_2/POT-EB/RGO 50:40:10 and MoS_2/POT-ES/RGO 50:40:10 before and after exposure to a light emitted by a halogen lamp, for 180 min. In Figures a-e, the colors black, red, green, blue, cyan, yellow, dark yellow, navy, purple, wine, olive, dark cyan, royal, orange, light yellow, gray, light magenta, light cyan and pink correspond to 0, 10, 20, 30, 40, 50, 60, 70, 80, 90, 100, 110, 120, 130, 140, 150, 160, 170 and 180 min. of exposing the samples to the light emitted by the halogen lamp.

In the initial state, the UV-VIS spectra of the MoS_2/POT-EB/RGO 50:40:10 and MoS_2/POT-ES/RGO 50:40:10 composites (Figures 8a and 8b) highlight a band with high absorbance located in the spectral range 250-400 nm and another with lower absorbance having a maximum at ~558 and 578 nm, respectively. Analysis of Figures 8c and 8d indicates that these bands belong to POT-EB and POT-ES, the UV-VIS spectra being characterized in the initial state by a band with high absorbance located in the spectral range 250-400 nm and another with lower absorbance having the maximum located at 604 and 614 nm, which by analogy with PANI were assigned to the π-π* transition in B, while the second one is attributed to π-π* transition in Q structure of POT-EB and the polaronic structure in POT-ES [42, 43]. The shift of the bands from 604 nm (Figure 8c) and 614 nm (Figure 8d) to 558 nm (Figure 8a) and 578 nm (Figure 8b) is due to the interaction of POT-EB and POT-ES, respectively, with MoS_2 and RGO, respectively. These shifts must consider the

View Article Online
DOI: 10.1039/D5NA01164C

pseudo-protonic doping of POT in the presence of MoS_2, which changes the effective conjugation length as well as the charge transfer between POT and RGO, leading to covalent functionalization of RGO with POT. A similar behavior is reported in the case of the MoS_2/ POT-ES/RGO 50:25:25 composite (Figure 8e). A careful analysis of Figure 8 indicates that in the UV-Vis spectra of the MoS_2/POT/RGO composites, the characteristic POT bands are predominantly observed, while the excitonic bands of MoS_2 are no longer visible. This is due to their overlap and masking by the intense absorptions of the polymer, the charge transfer between MoS_2–POT/RGO, and the fragmentation of the MoS_2 layers, which leads to the suppression of the individual optical signature of MoS_2 in the composite. A similar behavior is observed in the case of the binary POT/MoS_2 composites (Figure S3a and S3b). The exposure of the MoS_2/POT-EB/RGO 50:40:10 and MoS_2/ POT-ES/RGO 50:40:10 composites to UV light induces, in the first 40 minutes, a shift of the bands from 558 nm and 578 nm to 510 nm and 520 nm, respectively. This shift can be explained by taking into account the hydrogen bonds [43] established between the C=O group of NMP and N-H bonds of POT-EB/POT-ES, as well as the orientation of the dipoles of NMP vs. positive charges of POT-ES or the lone pair of amine groups of POT-EB, which induce changes in the orientation of macromolecular chains [44]. The above change is followed in the next 140 minutes by a gradual decrease in the absorbance of these bands until their disappearance. The same is not observed in the case of POT-EB and POT-ES. In these two cases, a shift of the maximum from 604 and 614 nm to 544 and 528 nm, respectively, is observed during the 180 min. of UV irradiation, with a slight change in the absorbance of this band. This shift can be explained considering Figure 5, where it is observed that in comparison with PANI-EB and PANI-ES, a decrease in conjugation degree of macromolecular compounds appears as a consequence of the charge transfer induced by 2D materials and of the torsion of the rings by the covalent coordinative binding of Mo to the imine groups of the quinoid rings of POT.

To verify whether the changes regarding the above electronic transitions are related to the polar or non-polar character of the solvent used, Figure 9 shows the evolution of the UV-VIS spectra of the MoS_2/POT-EB/RGO 50:40:10 composite in toluene and acetone, when the two solutions are exposed to light emitted by the halogen lamp.

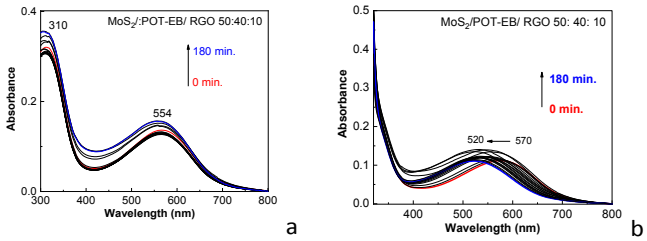

a b

Figure 9. UV-VIS spectra of the MoS_2/POT-EB/RGO 50:40:10 composite in toluene (a) and acetone (b).

The analysis of Figure 9 highlights that the UV-VIS spectra of the MoS_2/POT-EB/RGO composite in toluene and acetone are characterized by a band with high absorbance having a maximum at 310 nm and another located in the spectral range 400-800 nm with maxima at 554 nm (Figure 9a) and 570 nm (Figure 9b). Exposure to UV light of the MoS_2/POT-EB/RGO 50:40:10 composite in toluene does not induce significant variations in the position of the band at 554 nm (Figure 9a) while in the case of the MoS_2/POT-EB/RGO 50:40:10 composite in acetone it induces a shift of the band from 570 nm to 520 nm (Figure 9b), without significant variations in absorbance.

At this stage of our studies, a question remains, namely, what happens in the case of exposure to light emitted by the halogen lamp of the MoS_2/POT-EB/RGO composite in NMP? At present, we are tempted to put forward two hypotheses. The first one aims at a degradation of the macromolecular chain until obtaining very short fragments, some of them similar to the o-toluidine monomer, while the second hypothesis takes into account the generation of POT-LS. The blue curve in Figure 10a highlights that the o-toluidine band in the UV-VIS spectrum is located at 294 nm, a fact that indicates that a break of the macromolecular chain to entities similar to that of the monomer does not take place. To verify this second hypothesis, the solution of POT-EB and POT-ES, both dissolved in NMP, was interacted with the hydrazine solution, when one observes that, according to Figures 10a and 10b, the UV-VIS spectra are characterized only by a band having the maximum at 318 and 320 nm, respectively, very close to that of the two polymers

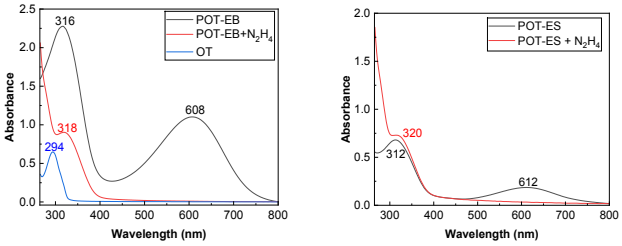

a b

Figure 10. UV-VIS spectra of: a) OT, POT-EB in NMP before and after interaction with hydrazine; and b) POT-ES in NMP before and after interaction with hydrazine.

The band in the 400-800 nm range in the case of POT-EB/POT-ES does not disappear due to the lack of a source of excited carriers of MoS_2 and a fast electron transporter such as RGO. A significant factor in the appearance of POT-ES is the photodegradation of NMP [45]. In this context, the second hypothesis should take into account the fact that NMP under UV light can be degraded by breaking the –C-C-C=O and N-CH_3 bonds with the formation of radicals of the type ·C=O, ·C-C=O, C_4H_3ON·, and CH_3· which can interact with the RGO sheets, leading to the transformation of RGO non-covalently functionalized with POT-pseudo-protonic doped in the presence of MoS_2, into RGO and POT-ES. A recent study demonstrated that NMP improves H_2S absorption performance and reduces the energy required for solvent regeneration compared to amine-only solutions [46]. Considering this reference and focusing on the products of reaction from Figure 5a, the following photochemical reactions can be envisaged to occur in the case of POT-pseudo-protonate in the presence of

MoS_2 and POT-LS covalently functionalized RGO in the presence of NMP (Figure 11):

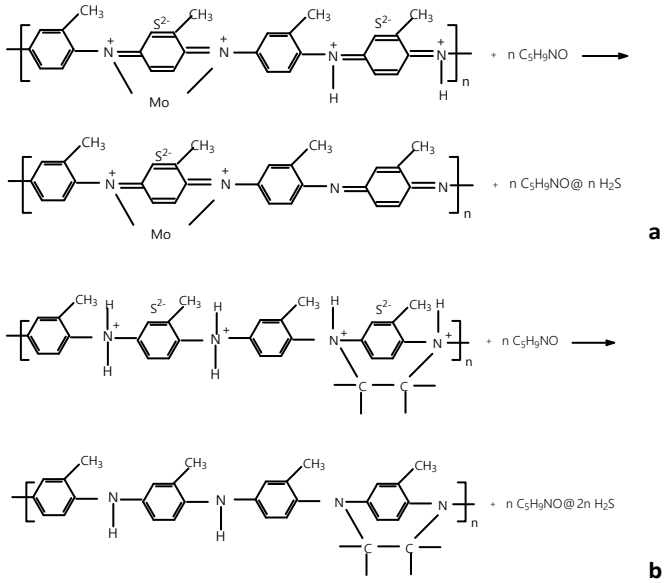

Figure 11. Photochemical reaction of POT pseudo-protonic doped in the presence of MoS_2 and POT-LS covalently functionalized RGO**.**

A schematic presentation of the photochemical reaction products of pseudo-protonic POT doped in the presence of MoS_2 and POT-LS covalently functionalized RGO is shown in Figure 12.

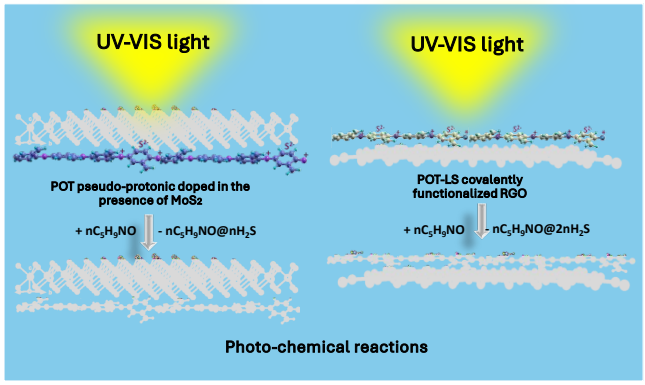

Figure 12. Schematic presentation of the photochemical reaction products of pseudo-protonic POT doped in the presence of MoS_2 and POT-LS covalently functionalized RGO.

In this stage of our study, we are tempted to attribute the variations observed in Figure 8 to the transformation of the RGO sheets non-covalently functionalized with POT pseudo-protonic doped in the presence of MoS_2 and POT-LS covalent functionalized RGO into RGO sheets modified with radicals of NMP, POT pseudo-protonic doped in the presence of MoS_2 and POT-LB covalent functionalized RGO, respectively. Additional information is shown in Figure 13, which shows the SERS spectra of the MoS_2/POT-ES/RGO 50:40:10 composite, after irradiation for 180 min., in the presence of Au nanoparticles with an average size of 10 nm. According to Figure 13a, when 40 µl of MoS_2/POT-ES/RGO 50:40:10 in NMP with a concentration of 0.2 mg/ml was added into 1 ml of Au nanoparticles, the SERS spectra show Raman lines belonging to: a) MoS_2 located at 374 and 407 cm^{-1} and b) POT having maxima at 623, 754, 860, 933, 1030, 1120, 1155-1173, 1228, 1309, 1370, 1431, 1458-1479-1510, and 1583 cm^{-1} belonging to the vibrational modes of the benzene ring deformation in LB-type structural units, N, N'-diphenyl-1 entities, 4-phenylenediamine (PCD) entities, C-H bending in the benzene ring, cation radical entities, benzene ring deformation, benzene ring deformation + C-H bending, C-H bending, C-N stretching, PCD entities, protonated or pseudo-protonated structure (-NX^+-, where X is H, Mo), C-C stretching + C-H stretching and C=C stretching in benzene ring [25, 26, 32, 34]. In our opinion, the presence of these Raman lines, peaked at 623, 754, 860, 933, 1120, 1155-1173, 1228, 1309, 1431, 1458-1479-1510, and 1583 cm^{-1}, confirms the structure of LB of POT covalently functionalized RGO, while the Raman line peaked at 1370 cm^{-1}, which is situated in the vicinity of the Raman lines of POT-ES (1358 cm^{-1}, Figure 3f) and its composites with MoS_2 and RGO (1336-1399 cm^{-1}, Figure 3b) confirms the structure of the state pseudo-protonic doped of POT.

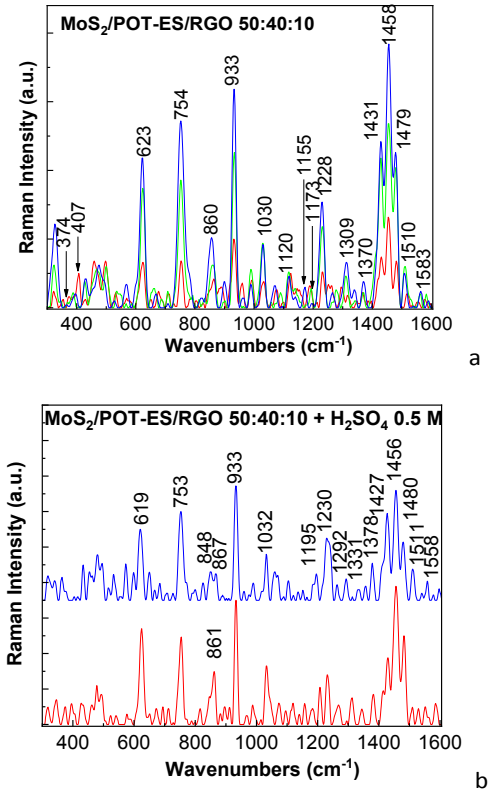

Figure 13. SERS spectra of the MoS_2/POT-ES/RGO 50:40:10 composite after 180 min. of exposure to light emitted by a halogen lamp; the red, green, and blue curves correspond to 40, 120, and 180 µl MoS_2/POT-ES/RGO composite in 1 ml of Au nanoparticles with an average size of 10 nm (a). Interaction of

View Article Online DOI: 10.1039/D5NA01064C

180 µl of MoS_2/POT-ES/RGO 50:40:10 composite with 120 µl (red curve) and 180 µl (blue curve) of 0.5 M H_2SO_4 (b).

Subsequent interaction of the MoS_2/POT-ES/RGO 50:40:10 composite solution after 180 min. of exposure to light emitted by a halogen lamp with 0.5 H_2SO_4 solution leads to: i) the shift of the Raman line from 1173 and 1309 cm^{-1} (Figure 13a) to 1195 and 1292 cm^{-1} (Figure 13b); b) the shift of the Raman line from 1370 cm^{-1} (Figure 13a) to 1378 cm^{-1} (Figure 13b) simultaneously with the increase in intensity, iii) the modification of the ratio between the intensities of the Raman lines located in the spectral range 1400-1500 cm^{-1} (Figure 13b) and iv) the shift of the Raman line from 1583 cm^{-1} (Figure 13a) to 1558 cm^{-1} (Figure 13b). These variations originate in the protonation of the reaction products of Figure 11, with their transformation into POT-LS, according to Figure 14.

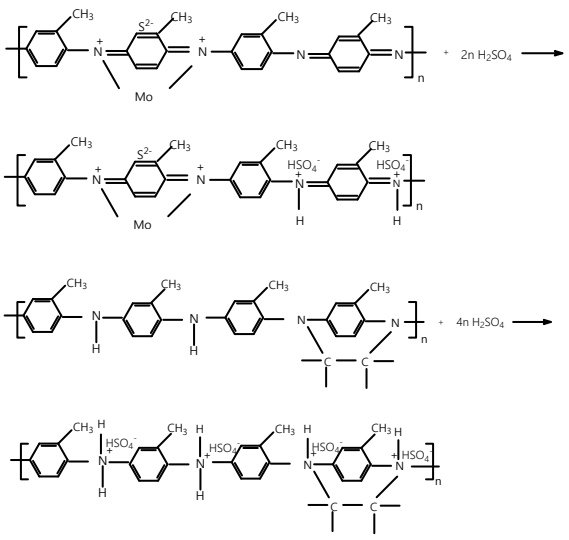

Figure 14. The interaction of H_2SO_4 with the reaction products of the MoS_2/POT-EB/RGO composite in NMP, after exposure to the light emitted by a halogen lamp for 180 min.

In our opinion, Figure 12 proves the protonic acid doping of the reaction products of the MoS_2/POT-EB/RGO composite in NMP, after exposure to the light emitted by a halogen lamp for 180 min., which in Figure 13b is marked by the Raman line peaked at 1378 cm^{-1}.

Conclusions

This work reports new results concerning the synthesis and optical properties of composites based on MoS_2, POT, and RGO. Binary and ternary composites were prepared. They were obtained through solid-state interaction between MoS_2, RGO sheets, and POT-EB/POT-ES. The conclusions are as follows:

i) Changes in Raman and FTIR spectra indicate that the interaction POT-ES with MoS_2 and RGO leads to a ternary composite of the type RGO non-covalently functionalized with POT pseudo-protonic doped in the presence of MoS_2, and a binary composite of the type RGO covalently functionalized with POT-LS. The interaction of POT-EB with MoS_2 and RGO leads to a ternary composite of the type RGO non-covalently functionalized with POT pseudo-protonic doped in the presence of MoS_2, and a binary composite RGO covalently functionalized with POT-LS. The formation of these composites involves the generation of additional defects in the MoS_2 sheets according to XRD studies.

ii) The UV-VIS spectra of the two macromolecular compounds, i.e., POT-EB and POT-ES, are characterized by two bands. The first one is situated in the spectral range 250-400 nm, and the second one has the maximum located at 604 and 614 nm, which were assigned to the π-π* transition in the benzene ring of POT-EB, and the π-π* transition in the quinoid structure of the polaronic structure of POT-ES. In the case of composites resulting from the solid-state interaction of the MoS_2 with RGO sheets and POT-EB or POT-ES, respectively, the band assigned to the π-π* transition in the benzene ring was reported to have a maximum at 558 and 578 nm. These changes are caused by pseudo-protonic doping of POT in the presence of MoS_2, which changes the effective conjugation length as well as the charge transfer between POT and RGO. As a result, covalent functionalization of RGO with POT occurs.

iv) The exposure to UV light of the mixture containing ternary and binary composites dissolved in NMP leads to a transformation of the RGO sheets non-covalently functionalized with POT pseudo-protonic doped in the presence of MoS_2, and POT-LS covalently functionalized RGO into RGO sheets, POT pseudo-protonic doped in the presence of MoS_2, and POT-LB covalently functionalized RGO. Studies by UV-VIS spectroscopy highlight this photochemical interaction by the disappearance of the band situated in the spectral range 400-800 nm and the presence of a band localized between 200 and 400 nm.

v) The interaction of H_2SO_4 with POT pseudo-protonic doped in the presence of MoS_2 and POT-LB covalently functionalized RGO leads to composites like those proposed in Figure 14.

Author contributions

Madalina Cercel: Visualization, Methodology, Investigation, Formal analysis. **Andreea Nila:** Visualization, Methodology, Investigation, Formal analysis. **Ion Smaranda:** Visualization, Methodology, Investigation, Formal analysis. **Andreea Androne:** Visualization, Methodology, Investigation, Formal analysis. **Teodora Burlanescu:** Visualization, Methodology, Investigation, Formal analysis. **Adam Lörinczi:** Visualization, Methodology, Investigation, Formal analysis. **Catalin Negrila:** Investigation, Methodology, Formal analysis, **Elena Matei:** Investigation, Methodology, Formal analysis, **Mihaela Baibarac:** Methodology, Investigation, Formal analysis, Writing-original draft, Writing-review & editing, Validation, Supervision, Resources, Project administration, Conceptualization.

Conflicts of interest

There are no conflicts to declare.

Declaration of competing interest

The authors declare that they have no known competing financial interests or personal relationships that could have appeared to influence the work reported in this paper.

Acknowledgements

This work is funded by the Core Program of the National Institute of Materials Physics, granted by the Romanian Ministry of Research, Innovation, and Digitization through the PC3-PN23080303.

References

1 K. Gopalakrishnan, A. Sultan, A. Govindaraj, C. N. R. Rao, Supercapacitors based on composites of PANI with nanosheets of nitrogen-doped RGO, BC1.5N, MoS_2, and WS_2, *Nano Energy* 2015, **12**, 52-58.

2 F.Y. Xiong, Z.Y. Cai, L.B. Qu, F.P. Zhang, Z.F. Yuang, O.K. Asare, et al., Three-dimensional crumpled reduced graphene oxide/MoS_2 nanoflowers: a stable anode for lithium-ion batteries, *ACS Applied Materials & Interfaces* 2015, **7**, 12625-12630.

3 T. Burlanescu, M. Cercel, I. Smaranda, A. Androne, I. Zgura, P.C. Ganea, C. Negrila, A. Lorinczi, C. Bartha, M. Baibarac, Optical, structural and electrical properties of composites based on MoS_2, WS_2 and poly(orto-toluidine), *Materials Today Communications* 2025, **46**, 112469.

4 X. Li, C.F. Zhang, S. Xin, Z.C. Yang, Y.T. Li, S.W. Zhang, P. Yao, Facile synthesis of MoS_2/Reduced graphene oxide @ polyaniline for high-performance supercapacitors, *ACS Applied Materials & Interfaces* 2016, **8**, 21373-21380.

5 D. Xie, D.H. Wang, W.J. Tang, X.H. Xia, Y.L. Zhang, X.L. Wang, C.D. Gu, J.P. Tu, Binder-free network-enabled MoS_2-PPY-rGO ternary electrode for high capacity and excellent stability of lithium storage, *J. Power Sources* 2016, **307**, 510-518.

6 W.W. Qin, Y. Li, Y.Q Teng, T. Qin, Hydrogen bond-assisted synthesis of MoS_2/reduced graphene oxide composite with excellent electrochemical performances for lithium and sodium storage, *J. Colloid Interface Science* 2018, **512**, 826-833.

7 G.S. Geleta, Z. Zhao, Z.X. Wang, A novel reduced graphene oxide/molybdenum disulfide/polyaniline nanocomposite-based electrochemical aptasensor for detection of aflatoxin B1, *Analyst* 2018, **143**, 1644-1649.

8 S.H. Li, Y.S. MA, Y.K. Lin, G. Xin, M.H. Wang, Z.H. Zhang, Z.Y. Liu, Electrochemical sensor based on a three dimensional nanostructured MoS_2 nanosphere-PANI/reduced graphene oxide composite for simultaneous detection of ascorbic acid, dopamine and uric acid, *RSC Advances* 2019, **9**, 2997-3003.

9 R.B. Choudhary, G. Mandal, MoS_2 decorated with graphene and polyaniline nanocomposite as an electron transport layer for OLED applications, *J. Mater. Sci.-Materials in Electronics* 2020, **31**, 1302-1316.

10 M.J. Shi, Z. Liu, S. Zhang, S.C. Liang, Y.T. Jiang, H. Bai, Z.M. Jiang, J. Chang, J. Feng, W.S. Chen, H.P. Yu, S.X. Liu, T. Wei, Z.J. Fan, A Mott-Schottky Heterogeneous Layer for Li-S Batteries: Enabling Both High Stability and Commercial-Sulfur Utilization, *Adv. Energy Mater*. 2022, **12**, 2103657.

11 G.H. Gupta, K. Mohan, S. Ghosh, S.S. Babu, R. Velyutham, G. Kapusetti, Label-Free detection of Poly-Cystic Ovarian Syndrome using a highly conductive 2D rGO/MoS_2/PANI nanocomposite based immunosensor, *Bioelectrochemistry* 2024, **158**, 108681. View Article Online DOI: 10.1039/D5NA01164G

12 J. Mariadhas, Y. Subramanian, G. Lakshmanan, .F Hamsath, J.H.R. Monica, M.T. Le, S.S.R. Inbanathan, A. Azad, Emerging robust heterostructure of flower-like (Calendula) MoS_2-warped rGO by polyaniline nanohybrid for antimicrobial and antipollution performances, *Catalysis Commun.* 2024, **187**, 106867.

13 S. Palsaniya, H.B. Nemade, A.K. Dasmahapatra, Synthesis of polyaniline/graphene/MoS_2 nanocomposite for high performance supercapacitor electrode, *Polymer* 2018, **150**, 150-158.

14 L.-Z. Bai, Y.-H. Wang, S.-S. Cheng, Li F, Z.-Y. Zhang and Y.-Q. Liu, Synthesis and Electrochemical Performance of Molybdenum Disulfide-Reduced Graphene Oxide-Polyaniline Ternary Composites for Supercapacitors, *Front. Chem*. 2018, **6**, 218.

15 S.P. Lonkar, V. Gupta, S.M. Alhassan, A. Schiffer, Three-dimensional MoS_x/polyaniline @graphene heteroaerogels as electrode materials for high-performance symmetric supercapacitors, *Energy Storage*, 2023, **5**, e416.

16 M. Baibarac, L. Mihut, G. Louarn, S. Lefrant, I. Baltog, Doping and Metallic-Support Effect Evidenced on SERS Spectra of Polyaniline Thin Films, *J. Polymer Sci.: Part B: Polymer Physics*, 2000, **38**, 2599-2609.

17 M. Scocioreanu, L. Mihut, M. Baibarac, I. Baltog, Photoluminescence decay time studies on ZnS in cubic and hexagonal phase and its mechanico-chemical interaction with polyaniline, *Physica Status Solidi B – Basic Solid State Physics* 2013, **250**, 1426-1431.

18 S. Nawez, Y. Khan, S. Khalid, M.A. Malik, M. Siddiq, Molybdenum disulfide (MoS_2) along with graphene nanoplates (GNPs) utilized to enhance the capacitance of conducting polymers (PANI and PPY), *RSC Adv*. 2023, **13**, 28785-28797.

19 J. Dai, Y. Luo, J. Zhang, H. Xie, C. Guo, A. Zhu, Y. Xu, M. Fan, C. Yuan, L. Dai, Effect of morphology and phase engineering of MoS2 on electrochemical properties of carbon nanotube/polyaniline @MoS_2 composites, *J. Colloid Interface Sci*. 2021, **590**, 591-600.

20 H. Ahmad, I.I. Bin Sharfan, R.A. Khan, A. Alsalme, 3D nanoarchitecture of polyaniline – MoS_2 hybrid material for Hg (II) adsorption properties, *Polymers* 2020, **12**, 2731.

21 - M. Madeshwaran, K.S. Rajni, M. Ulaganathan, Polyaniline @MoS_2: An organic and inorganic hybrid framework for asymmetric supercapacitor applications, *Materials Today Chem*. 2024, **42**, 102390.

22 C.I. Idumah, A review on polyaniline and graphene nanocomposites for supercapacitors, *Polymer – Plastics Technolgy and Materials* 2022, **61**, 1871-1907.

23 T. Burlanescu, M. Văduva, A. Androne, M. Paraschiv, M. Cercel, C. Negrila, M. Baibarac, Composites based on poly(ortho-toluidine) and reduced graphene oxide: from synthesis to optical characterization and potential applications in the energy storage field, *RSC Adv*. 2026 accepted, DOI: 10.1039/d6ra00288a.

24 M. Saliba, J. P. Atanas, T. M. Howayek and R. Habchi, Molybdenum disulfide, exfoliation methods and applications to photocatalysis: a review, *Nanoscale Adv.*, 2023, **5**, 6787

25 S.Quillard, G. Louarn, S. Lefrant; A.G. MacDiarmid, Vibrational analysis of polyaniline: A comparative study of leucoemeraldine, emeraldine, and pernigraniline bases, *Phys. Rev. B* 1994, **50**, 12496-12508.

26 M. Lapkowski, K. Berrada, S. Quillard, G. Louarn, S. Lefrant, A Pron, Electrochemical oxidation of polyaniline in nonaqueous electrolytes – In-situ Raman spectroscopic studies, *Macromolecules* 1995, **28**, 1233-1238.

27 C. Lee, H. Yan, I.E. Brus, T.E. Heinz, J. Hone, S. Reey, Anamalous lattice vibrations of single and few layer MoS_2, *ACS Nano* 2010, 4, 2695-2700.

28 L.M. Malard, M.A. Pimenta, G. Dresselhaus, M.S. Dresselhaus, Raman spectra in graphene, *Phys. Rep*. 2009, **473**, 51-87.

29 L.G. Cancado, A. Jorio, E.H. Martins Ferreira, F. Stavale, C. A. Achete, R. B. Capaz, M.V.O. Moutinho, A. Lombardo, T.S. Kulmala, A.C. Ferrari, Quantifying defects in graphene via Raman spectroscopy at different excitation energies, *Nano Letters* 2011, **11**, 3190-3196.

30 I. Smaranda, A.M. Benito, W.K. Maser, I. Baltog, M. Baibarac, Electrochemical grafting of reduced graphene oxide with polydiphenylamine doped with heteropolyanions and its optical properties, *J. Phys. Chem. C* 2014, **118**, 25704-25717

31 M. Baibarac, M. Stroe, S.N. Fejer, Vibrational and photoluminescence properties of polydiphenylamine doped with silicotungstic acid heteropolyanions and their composites with reduced graphene oxide, *J. Molec Struct.* 2019, 1184, 25.

32 S. Quillard, G. Louarn, J. P. Buisson, S. Lefrant, J. Masters, A.G. MacDiarmid, Vibrational analysis of the reduced form of polyaniline: the leucoemeraldine base, Synth. Met. 1992, **49-50**, 525-530.

33 M.R. Raj, S. Anandan, M. Zhou, M. Ashokkumar, A facil one-step synthesis of hollow polydiphenylamine, *Int. J. Polym. Mater*. 2013, **62**, 23-27.

34 H. de Santana, F.C. Dias, Characterization and properties of polydiphenylamine electrochemically modified by iodide species, *Mater. Chem. Phys*. 2003, **82**, 882e886.

35 K. Ataka, M. Osawa, In situ infrared study of water-sulfate coadsorption of gold (111) in sulfuric acid solutions, *Langmuir* 1998, **14**, 951-959.

36 Z. Ping, G.E. Nauer, H. Neugebauer, J. Theiner, A. Neckel, In situ Fourier transform infrared attenuated total reflection (FTIR-ATR) spectroscopic investigation on the base-acid transitions of leucoemeraldine, *Electrochim. Acta* 1997, **42**, 1693-1700.

37 M. V. Olenchuk, U.K. Afonina, O.P. Gnatyuk, V.V. Strelchuk, A.S. Nikolenko, G.I. Dovbeshko, Heat annealing influences the optical properties of 2D-MoS_2 nanoparticles, *Molec. Cryst. Liq. Cryst*. 2022, **749**, 1-8.

38 S. Golczak, A. Kanciurzewska, M. Fahlman, K. Langer, J.J. Langer, Comparative XPS surface study of polyaniline thin films, *Solid State Ionics* 2008, 178, 2234-2239.

39 M.M. Mahat, D. Mawad, G.W. Nelson, S. Fearn, R. G. Palgrave, D. J. Payne, M.M. Stevens, Elucidating the protonation of polyaniline films by X-ray photoelectron spectroscopy, *J. Mater Chem. C* 2015, **3**, 7180-7186.

40 Y. Zhang, J. Liu, Y. Pan, K. Luo, J. Yu, Y. Zhang, K. Jla, H. Yln, H. Tlan, Z. Wu, The evolution of MoS2 properties under oxygen plasma treatment and its application in MoS_2 based devices, *J. Mater Sci. Mater Electron*. 2019, **30**, 18185-18190.

41 N.H. Turmer, A.M. Singlet, Determination of peak position and areas from wide-scan XPS spectra, *Surf. Interface Anal*. 1990, **15**, 215-222.

42 A. A. Salem, B. N. Grgur, The influence of the polyaniline initial oxidation states on the corrosion of steel with composite coatings, *Polymer in Organic Coatings* 2018, **119**, 138-144.

43 P. J. Dysona, P. G. Jessopb, Solvent effects in catalysis: rational improvements of catalysts via manipulation of solvent interactions, *Catal. Sci. Technol*., 2016, **6**, 3302.

44 M. Isanejad, N. Azizi, T. Mohammadi, Pebax membrane for CO_2/CH_4 separation: Effects of various solvents on morphology and performance, *J. Appl. Polym. Sci*. 2017, 44531.

45 P. Kumar, S. Verma, R. Kaur, J. Papac, H. Kusic, U. L. Stangar, Enhanced photo-degradation of N-methyl-2-pyrrolidone (NM): influence of matrix components, kinetic study and artificial neural network modelling, J. Hazardous Mater. 2022, **434**, 128807.

46 A.S. Farooqi, R.M. Ramii, S.S. M. Lock, A.S. Farooqi, M. Z. Shahid, S.M.W Hasmain, N. Hira, B. Abdullah, Removal of carbon dioxide and hydrogen sulfide from natural gas using a hybrid solvent of monoethanolamine and N-methyl-2-pyrrolidone, *ACS Omega* 2024, **4**, 25704-25714.

View Article Online
DOI: 10.1039/D5NA01164G

Data Availability Statement

The data that support the findings of this study are available from the corresponding author, Dr. Mihaela Baibarac, upon reasonable request.